Active Class E Rectifier for DC Output Voltage Regulation in Megahertz Wireless Power Transfer Systems

Ming Liu, *Member, IEEE,* Jibin Song, *Student Member, IEEE,* Chengbin Ma, *Senior Member, IEEE*

***Abstract*—In real applications, it is usually desirable to have a regulated dc output voltage from a wireless power transfer (WPT) system. This voltage regulation is especially necessary because of possible variation in coupling coil relative position and thus a changing mutual inductance. For WPT systems working at megahertz (MHz), Class E rectifiers are known to be advantageous thanks to their simple configuration and soft-switching operation. This paper proposes a new Class-E-based active rectifier. This rectifier is capable to simultaneously perform high-efficiency rectification and output voltage regulation, but without the need to have an additional regulating circuit. Analytical derivations and analysis are provided to explain the operation principle in detail. Guidance is also developed for a balanced design of parameters, which compromises among different criteria. Final experiments validate the analytical analysis and dc output voltage regulation via the active rectifier. With the duty cycle control of the rectifier, a constant output voltage (10 V) can be maintained under a varying mutual inductance coefficient and with an over 92% rectifying efficiency.**

***Index Terms*—Wireless power transfer, magnetic resonance coupling, active rectifier, Class E topology, output voltage regulation.**

I. Introduction

There was a continuous development in wireless power transfer (WPT) technologies, as observed in recent years. WPT has been widely applied to charge wearable devices, cellphones, household appliances, and even electrical vehicles, etc. Most of present WPT systems operate in kilohertz (kHz) frequency band. Significant efforts were made to improve the performance of KHz systems, such as through improvements in coil design, compensation topology, and control [1]–[4]. At the same time, A higher operating frequency, such as several megahertz (MHz), is known to be able to further improve spatial freedom of the power transfer, namely a longer transfer distance and better tolerance to the coil misalignment [5], [6]. A higher operating frequency is also beneficial to enable more compact and lighter WPT systems. However, due to limited high-frequency performance of today's devices, mostly the switches, the MHz WPT is now considered to be suitable for transferring a medium amount of power. Meanwhile, MHz WPT at kW level has been studied using wide bandgap devices and with improved circuit topology [7]. Similar to its counterpart, the KHz WPT, the MHz WPT is under a rigorous research and development phase. Many investigations have been conducted on circuit, design and optimization at both component and system levels [8]–[10].

In real applications, a regulated dc output voltage from the WPT system is usually desirable. This practical requirement is important to maintain functionality of the overall charging systems. However, variation in relative position of the coupling coils (i.e., mutual inductance) is unavoidable in many cases. This uncertainty will lead to a changing dc output voltage. Impedance compression topologies and feedback-based control have been proposed to suppress the influence of the changing mutual inductance [11], [12]. A thinned-out method (i.e., replacement of pulse patterns) was proposed to regulate the dc output voltage or power of the Class E rectifier, which improves efficiency for low output voltage [13]. In existing solutions, the voltage regulator or control pulse modulation are usually required to regulate the dc output voltage of the WPT systems. This increases size, weight, power dissipation, and control complexity, particulary on the receiving side (e.g., a mobile device). New solutions are expected to simplify the circuit configuration; while, at the same time, provide output voltage regulation capability. This paper proposes a new active Class E rectifier to simultaneously perform high-efficiency rectification at MHz and dc output voltage regulation, but without the need of an additional regulating circuit. This proposed active rectifier is based on a classical Class E rectifier, which is well known for its high efficiency when operating at MHz [14].

This paper is organized as follows. In section II, circuit model and analytical analysis are first provided to explain four operating modes of the active Class E rectifier. Key waveforms and rectifier input impedance are given to verify the operation principle and tunable rectifier impedance through duty cycle control of a newly added switch. Guidance is also developed to select the rectifier design parameters taking into account the tradeoffs among different criteria. In section III, a scheme of the rectifier dc output voltage regulation is further discussed and verified through analytical analysis. Finally, in section IV, an experimental 6.78 MHz WPT system is built up employing

Manuscript received Dec. 5, 2018; revised Mar. 23, 2019; accepted May 12, 2019. This work was supported by the Shanghai Natural Science Foundation under Grant 16ZR1416300.

M. Liu is with Department of Electrical Engineering, Princeton University, Princeton, NJ 08544, USA (e-mail: ml45@princeton.edu).

J. Song and C. Ma are with the University of Michigan-Shanghai Jiao Tong University Joint Institute, Shanghai Jiao Tong University, Shanghai 200240, China (e-mail: jibinsong@sjtu.edu.cn; chbma@sjtu.edu.cn).

the proposed active Class E rectifier. The experiment results validate the above analytical analysis, high efficiency operation of the active rectifier, and its dc output voltage regulation capability.

II. Active Class E Rectifier

Fig. 1 shows circuit model of a classical Class E half-wave rectifier, in which the diode parasitic capacitor is absorbed into the shunt capacitor C_r. The rectifier is driven by a sinusoidal current and the current through the filter inductor L_f equals to the dc output current of the rectifier. Thus C_r and D_r are alternatively driven by the combination of the sinusoidal current and the dc output current. This combination of the two currents determines the waveforms of the diode voltage and capacitor voltage. The dc output voltage of the rectifier equals to the average voltage across the diode. Thanks to its current-driven operation, the rectifier can be applied in WPT systems with the series resonance on the receiving side. From this basic topology, a new active Class E rectifier is developed. Its operation principle and design guidance are discussed in detail as follows.

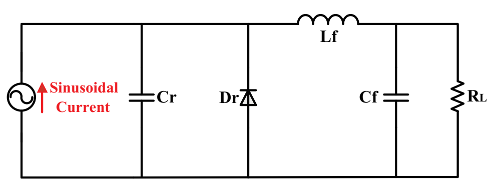

Fig. 1. Classical current-driven Class E rectifier.

A. Circuit Analysis

Fig. 2(a) shows the proposed active Class E rectifier. It consists of a switch Q_r, a diode D_r, shunt capacitors C_r, C_{Q_r}, C_{D_r}, a RF chock inductor L_f, a filter capacitor C_f, and a dc load R_L. Note that C_{Q_r} and C_{D_r} absorb the parasitic capacitors of Q_r and D_r, respectively. They help to achieve the soft-switching operation of Q_r and D_r. In the classical Class E rectifier in Fig. 1, the value of C_r is an important parameter. It determines the rectifier input impedance (i.e., load impedance of the receiving coil), and thus efficiency and power transfer capability of the coupling coils. In the proposed active Class E rectifier, the switch Q_r is newly added. Duty cycle control of Q_r makes it possible to influence the on/off status of the diode D_r. This provides a new degree of freedom to actively tune the rectifier input impedance and eventually the dc output voltage of the WPT system, V_o.

Equivalent circuit models of the proposed active rectifier are given in Fig. 2(b)-(e). They correspond to four operation modes in total. In the subfigures, i_{rec} is rectifier input current; I_o is rectifier dc output current; i_{D_r} and $i_{C_{D_r}}$ are currents through diode D_r and its shunt capacitor C_{D_r}; i_{Q_r} and $i_{C_{Q_r}}$ are currents through switch Q_r and its shunt capacitor C_{Q_r}; v_{Q_r} and v_{D_r} are voltages across Q_r and D_r; v_{rec} and V_o are rectifier ac input voltage and dc output voltage. In order to analytically discuss operation principle of a Class-E-based rectifier, following assumptions are usually common:

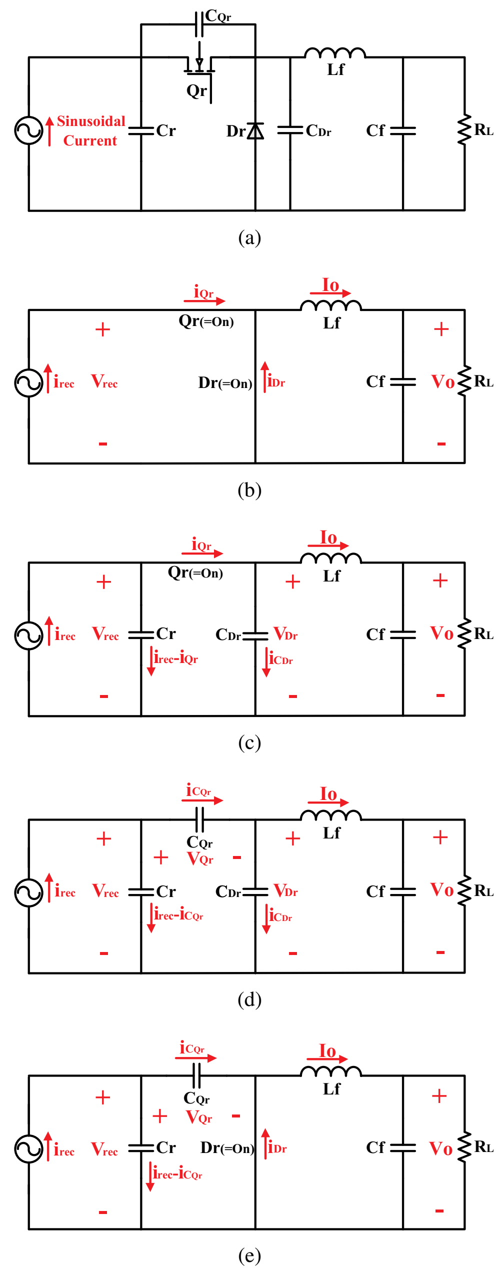

Fig. 2. Active Class E rectifier. (a) Circuit model. (b) Mode 1. (c) Mode 2. (d) Mode 3. (e) Mode 4.

1) a sinusoidal current source drives the rectifier;
2) diode forward voltage drop is neglectable;
3) current through the filter inductor L_r is constant, and equals the dc output current I_o;
4) output ripple voltage is sufficiently small, namely a constant dc output voltage V_o.

Assume the rectifier input current i_{rec} is

$$i_{rec} = I_m \sin(\omega t + \phi_{rec}), \tag{1}$$

where I_m is amplitude, ϕ_{rec} is initial phase, and ω is a target operating frequency. As summarized in Table I, the four operation modes correspond to four different time intervals and on/off states of Q_r and D_r, respectively. Here D_2 is the actual duty cycle of the switch Q_r. D_1 and D_3 are equivalent duty cycles that define mode transition timing of the active rectifier. They are determined by D_2 and circuit parameters. Fig. 3 further summarizes the definitions of D_1, D_2, and D_3. The three duty cycles are respectively defined to represent the time intervals from $\omega t = 0$ to the ending times of mode 1, mode 2, and mode 3. Through the control of the actual duty cycle D_2, the voltages across the capacitors (C_r, C_{Q_r}, C_{D_r}) change and thus the output voltage can be regulated.

TABLE I
FOUR OPERATION MODES.

Mode	Interval	Q_r	D_r
1	$(0,\ 2\pi D_1]$	on	on
2	$(2\pi D_1,\ 2\pi D_2]$	on	off
3	$(2\pi D_2,\ 2\pi D_3]$	off	off
4	$(2\pi D_3,\ 2\pi]$	off	on

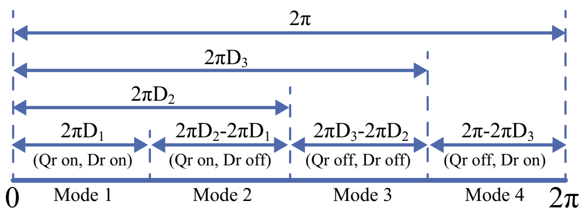

Fig. 3. Definitions of duty cycles, D_1, D_2, and D_3.

In the following analytical derivations, the rectifier input voltage, the MOSFET voltage and current, and the diode voltage and current, during the modes 1–4 are separately calculated. The results are used to plot the voltage and current waveforms of the rectifier, analyze the operation principle and develop design of parameters. They also help derive the input impedance of the rectifier, and eventually establish the relationship between the dc output voltage of the WPT system and the three duty cycles [refer to Sections II-B and III]. In mode 1 ($0 < \omega t \leq 2\pi D_1$), both Q_r and D_r are in on state. As shown in Fig. 2(b), the following relationship exists,

$$i_{D_r} = I_o - i_{rec}. \tag{2}$$

i_{D_r} is equal to zero when $\omega t = 2\pi D_1$, namely equal i_{rec} and I_o. Then, I_o can be expressed as

$$I_o = I_m \sin(2\pi D_1 + \phi_{rec}). \tag{3}$$

In mode 2 ($2\pi D_1 < \omega t \leq 2\pi D_2$), Q_r and D_r are in on and off states, respectively. As shown in Fig. 2(c), the respective currents through C_r, C_{D_r}, and Q_r are

$$i_{C_r} = i_{rec} - i_{Q_r}, \tag{4}$$

$$i_{C_{D_r}} = i_{Q_r} - I_o, \tag{5}$$

$$i_{Q_r} = \frac{C_{D_r}}{C_r + C_{D_r}} i_{rec} + \frac{C_r}{C_r + C_{D_r}} I_o. \tag{6}$$

Thus v_{Dr} and v_{rec} are

$$\begin{aligned} v_{Dr} = v_{rec} = &\frac{1}{\omega(C_r + C_{Dr})}[I_m \cos(2\pi D_1 + \phi_{rec}) \\ &- I_m \cos(\omega t + \phi_{rec}) + 2\pi D_1 I_o - \omega t I_o]. \end{aligned} \tag{7}$$

In mode 3 ($2\pi D_2 < \omega t \leq 2\pi D_3$), Q_r and D_r are both in the off state. As shown in Fig. 2(d), voltages across Q_r and D_r are

$$v_{Qr} = \frac{1}{\omega C_{Qr}} \int_{2\pi D_2}^{\omega t} i_{C_{Q_r}} d\omega t, \tag{8}$$

$$v_{Dr} = v_{D_r,ini} + \frac{1}{\omega C_{Dr}} \int_{2\pi D_2}^{\omega t} (i_{C_{Q_r}} - I_o) d\omega t, \tag{9}$$

where the initial voltage is [refer to (7)]

$$\begin{aligned} v_{D_r,ini} = &\frac{1}{\omega(C_r + C_{Dr})}[I_m \cos(2\pi D_1 + \phi_{rec}) \\ &- I_m \cos(2\pi D_2 + \phi_{rec}) + 2\pi D_1 I_o - 2\pi D_2 I_o]. \end{aligned} \tag{10}$$

Note that v_{D_r} is zero when ωt is $2\pi D_3$, and v_{rec} is

$$v_{rec} = v_{D_r,ini} + \frac{1}{\omega C_r} \int_{2\pi D_2}^{\omega t} (i_{rec} - i_{C_{Qr}}) d\omega t. \tag{11}$$

Note that v_{rec} = v_{D_r} + v_{Q_r}. Thus, from the above equations it can be found that

$$\begin{aligned} \int_{2\pi D_2}^{\omega t} i_{C_{Qr}} d\omega t = &\frac{1}{\frac{1}{\omega C_r} + \frac{1}{\omega C_{Qr}} + \frac{1}{\omega C_{Dr}}} \left\{ \frac{1}{\omega C_r}[I_m \cos(2\pi D_2 \right. \\ &\left. + \phi_{rec}) - I_m \cos(\omega t + \phi_{rec})] + \frac{1}{\omega C_{Dr}}(\omega t I_o - 2\pi D_2 I_o) \right\}. \end{aligned} \tag{12}$$

In mode 4 ($2\pi D_3 < \omega t \leq 2\pi$), Q_r and D_r are in off and on states, respectively. Again, as shown in Fig. 2(e), currents through C_{Q_r} and C_r can be derived as

$$i_{C_{Q_r}} = \frac{C_{Q_r}}{C_{Q_r} + C_r} i_{rec}, \tag{13}$$

$$i_{C_r} = \frac{C_r}{C_{Q_r} + C_r} i_{rec}. \tag{14}$$

Similarly v_{rec}, which equals v_{Q_r}, is

$$\begin{aligned} v_{rec} &= v_{Q_r,ini} + \frac{1}{\omega C_r} \int_{2\pi D_3}^{\omega t} (i_{rec} - i_{C_{Q_r}}) d\omega t, \\ &= v_{Q_r,ini} + \frac{I_m[\cos(2\pi D_3 + \phi_{rec}) - \cos(\omega t + \phi_{rec})]}{\omega(C_r + C_{Q_r})}, \end{aligned} \tag{15}$$

where [refer to (12)]

$$v_{Q_r,ini} = \frac{1}{\omega C_{Q_r}} \int_{2\pi D_2}^{2\pi D_3} i_{C_{Q_r}} d\omega t. \tag{16}$$

Again v_{rec} is zero when $\omega t = 2\pi$. Finally, the rectifier dc output voltage V_o equals the average voltage across D_r,

$$V_o = v_{D_r,avg} = \frac{1}{2\pi} \left(\int_{2\pi D_1}^{2\pi D_2} v_{D_r} d\omega t + \int_{2\pi D_2}^{2\pi D_3} v_{D_r} d\omega t \right), \tag{17}$$

namely average non-zero v_{D_r} during modes 2 and 3 [refer to (7)(9)].

Table III summarizes the calculation results with a changing D_2, 0.1–1, and example circuit parameters in Table II. It can be seen that the equivalent duty cycles D_1 and D_3 increase with a bigger D_2. Naturally, when D_2 equals one, D_3 also

TABLE II
EXAMPLE CIRCUIT PARAMETERS.

I_m (A)	C_r (pF)	C_{Q_r} (pF)	C_{D_r} (pF)	R_L (Ω)
2	400	400	400	10

TABLE III
CALCULATION RESULTS.

D_2	D_1	D_3	ϕ_{rec} (rad)
0.1	0.095	0.627	-0.314
0.2	0.146	0.665	-0.606
0.3	0.197	0.701	-0.889
0.4	0.250	0.741	-1.170
0.5	0.301	0.786	-1.449
0.6	0.352	0.836	-1.723
0.7	0.399	0.887	-1.990
0.8	0.443	0.938	-2.239
0.9	0.478	0.980	-2.449
1	0.493	1	-2.544

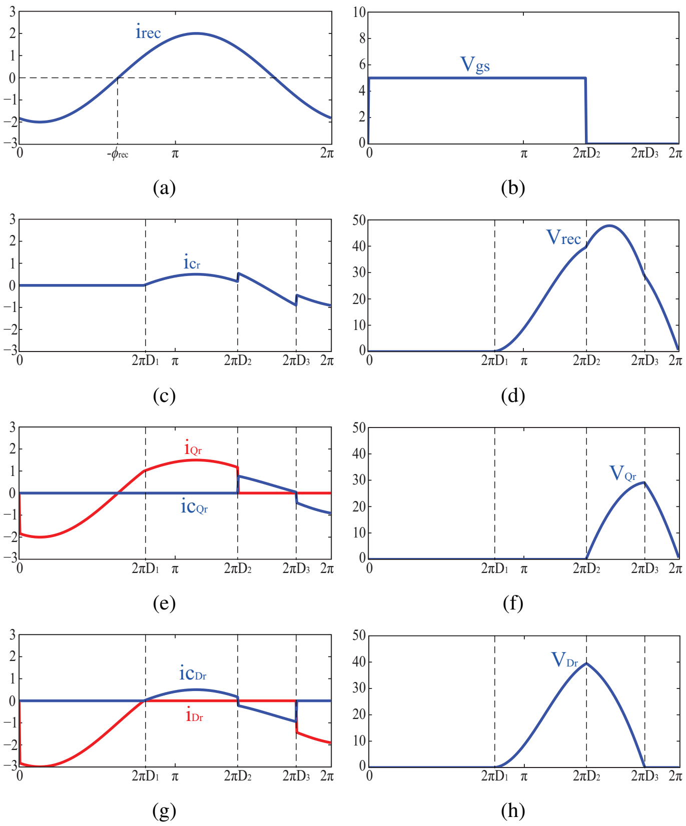

Fig. 4. Calculated key waveforms. (a) i_{rec} (A). (b) V_{gs} (V). (c) i_{C_r} (A). (d) v_{rec} (V). (e) i_{Q_r} (red) and $i_{C_{Q_r}}$ (blue) (A). (f) v_{Q_r}. (g) i_{D_r} (red) and $i_{C_{D_r}}$ (blue) (A). (h) v_{D_r} (V).

equals one and the rectifier simply works as a classical current-driven half-wave Class E rectifier [see Fig. 1]. The largely changed ϕ_{rec} also indicates a wide tunable range of rectifier input reactance. Key waveforms of the active Class E rectifier are shown in Fig. 4, in which v_{gs} is the gate-driving voltage of Q_r. Note that the rectifier input voltage v_{rec} combines v_{Q_r} and v_{D_r}, and peak v_{Q_r} and v_{D_r} occur when $\omega t = 2\pi D_3$ and $\omega t = 2\pi D_2$, respectively. The waveforms of v_{Q_r} and v_{D_r} also demonstrate the soft-switching operation of Q_r and D_r.

B. Input Impedance Derivation

The sinusoidal rectifier input current i_{rec} makes it possible to derive input impedance of the proposed active Class E rectifier Z_{rec} at the operating frequency ω,

$$Z_{rec} = R_{rec} + jX_{rec}. \tag{18}$$

Note that the above R_{rec} and X_{rec} are defined at the operating frequency. Fundamental component of the rectifier input voltage, $v_{rec,\omega}$, can be represented as

$$\begin{aligned} v_{rec,\omega} &= v_{R_{rec}} + v_{X_{rec}} \\ &= V_{m,R_{rec}} \sin(\omega t + \phi_{rec}) + V_{m,X_{rec}} \cos(\omega t + \phi_{rec}), \end{aligned} \tag{19}$$

where $V_{m,R_{rec}}$ and $V_{m,X_{rec}}$ are the amplitudes of $v_{R_{rec}}$ and $v_{X_{rec}}$, respectively. The input resistance and reactance of the rectifier, R_{rec} and X_{rec}, can then be solved via the trigonometric Fourier series for real-valued signals,

$$R_{rec} = \frac{V_{m,R_{rec}}}{I_m} = \frac{1}{\pi I_m}\int_0^{2\pi} v_{rec}\mathrm{sin}(\omega t + \phi_{\mathrm{rec}})\mathrm{d}\omega\mathrm{t}, \tag{20}$$

$$X_{rec} = \frac{V_{m,Xrec}}{I_m} = \frac{1}{\pi I_m}\int_0^{2\pi} v_{rec}\mathrm{cos}(\omega t + \phi_{rec})d\omega t. \tag{21}$$

As shown above, R_{rec} and X_{rec} are determined by the rectifier input voltage v_{rec} at modes 2–4 (v_{rec} = 0 at mode 1), namely the three duty cycles, D_1, D_2, and D_3. The non-zero v_{rec} in modes 2–4 are derived in (7), (11), and (15). R_{rec} and X_{rec} can then be accordingly calculated in a piecewise manner using the above two equations, (20) and (21).

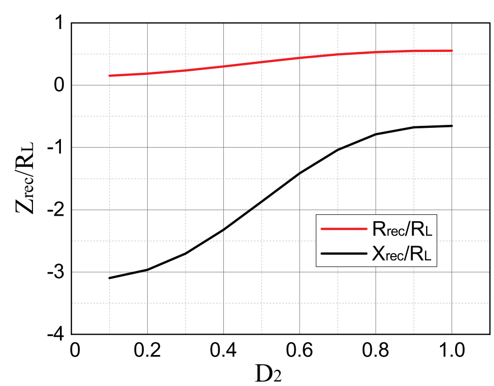

Fig. 5. Normalized rectifier input impedance versus D_2.

Fig. 5 shows an example of a normalized rectifier input impedance, R_{rec}/R_L and X_{rec}/R_L, when D_2 changes from 0.1 to 1. The circuit parameters in Table II are applied again. The figure especially demonstrates that the input reactance X_{rec} is largely tuned through the duty cycle control of the switch, i.e., modulation of D_2. This possibility can be fully utilized to achieve output voltage regulation of the MHz WPT systems, as discussed in Section III. Note that with reactance tuning capability, this active rectifier can be also used for reactance compensation in high-frequency WPT systems or radio-frequency systems.

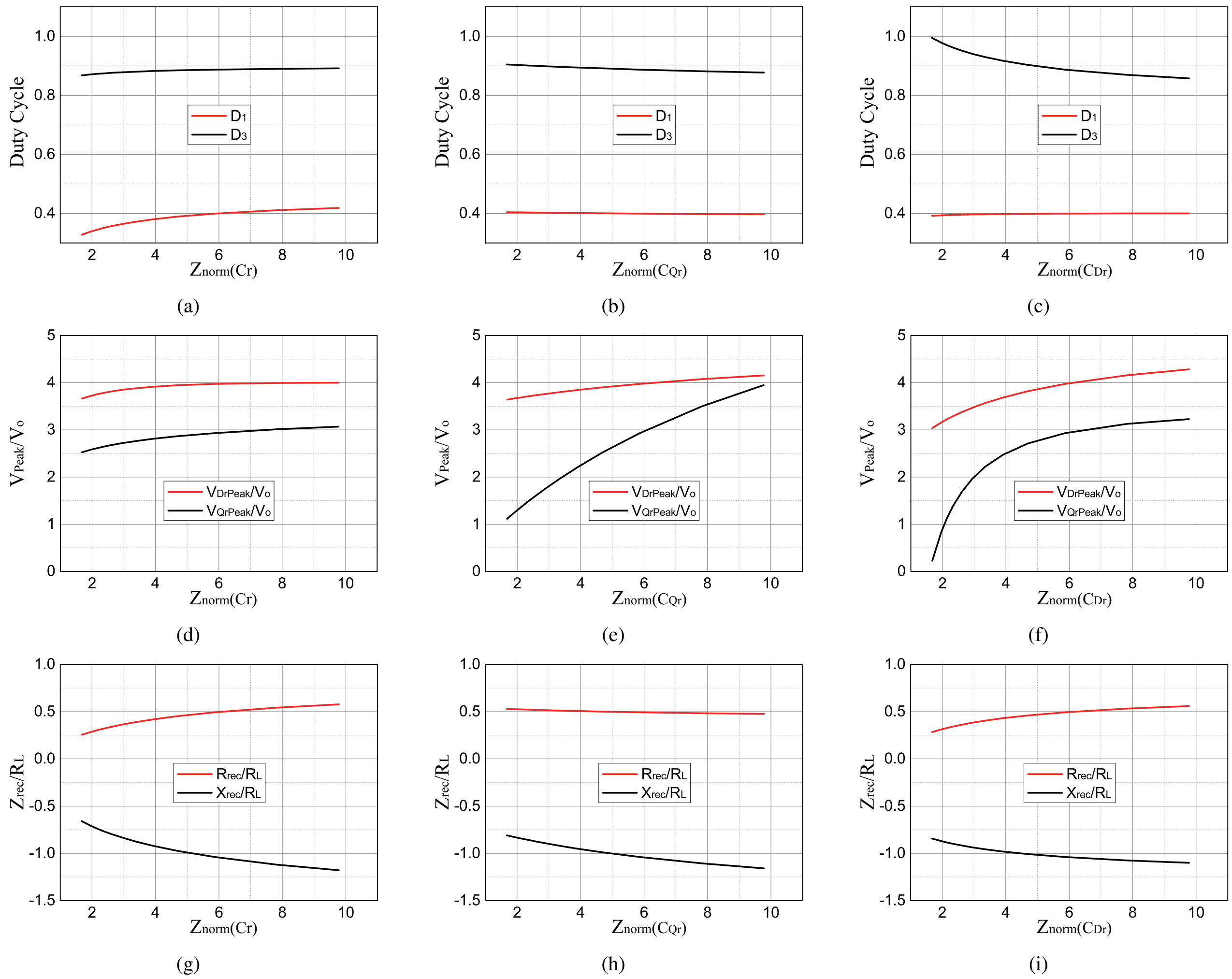

Fig. 6. Influences of C_r, C_{Q_r}, and C_{D_r}. (a) D_1 and D_3 versus $Z_{norm}(C_r)$. (b) D_1 and D_3 versus $Z_{norm}(C_{Q_r})$. (c) D_1 and D_3 versus $Z_{norm}(C_{D_r})$. (d) $V_{Q_r,peak}/V_o$ and $V_{D_r,peak}/V_o$ versus $Z_{norm}(C_r)$. (e) $V_{Q_r,peak}/V_o$ and $V_{D_r,peak}/V_o$ versus $Z_{norm}(C_{Q_r})$. (f) $V_{Q_r,peak}/V_o$ and $V_{D_r,peak}/V_o$ versus $Z_{norm}(C_{D_r})$. (g) Z_{rec}/R_L versus $Z_{norm}(C_r)$. (h) Z_{rec}/R_L versus $Z_{norm}(C_{Q_r})$. (i) Z_{rec}/R_L versus $Z_{norm}(C_{D_r})$.

C. Design Guidance

As explained above, the three capacitors, C_r, C_{Q_r}, and C_{D_r}, play a very important role in the operation of the active Class E rectifier. Fig. 6, which applies the example circuit parameters in Table II, shows their influences on

1) the two equivalent duty cycles (D_1 and D_3);
2) ratio of peak voltages of Q_r and D_r to rectifier output voltage ($V_{Q_r,peak}/V_o$ and $V_{D_r,peak}/V_o$);
3) the normalized input impedance (R_{rec}/R_L and X_{rec}/R_L).

For generality, in Fig. 6 the below normalized impedances are respectively changed to investigate the influences of the capacitors,

$$Z_{norm}(C_{\{\bullet\}}) = \frac{1}{\omega R_L C_{\{\bullet\}}}, \tag{22}$$

where $C_{\{\bullet\}}$ represents C_r, C_{Q_r}, or C_{D_r}. Important observations are as follows:

1) Fig. 6(a)–(c): the small $Z_{norm}(C_{Q_r})$ and $Z_{norm}(C_{D_r})$ lead to a high D_3. As shown in Fig. 4(f), it causes a short duration of mode 4 (i.e., $2\pi D_3 < \omega t < 2\pi$). The rapid decrease of v_{Q_r} is obviously unfavorable for the soft-switching operation of the rectifier.
2) Fig. 6(d)–(f): Peak voltages of D_r and Q_r are calculated when $\omega t = 2\pi D_2$ and $\omega t = 2\pi D_3$ respectively [see Fig. 4(f) and (h)]. Generally, smaller $Z_{norm}(C_{Q_r})$ and $Z_{norm}(C_{D_r})$ result in lower $V_{Q_r,Peak}/V_o$ and $V_{D_r,Peak}/V_o$, and thus lower voltage stress on Q_r and D_r.
3) Fig. 6(g)–(i): Higher nominal impedances enable a higher rectifier input reactance, X_{rec}. This indicates a wider tunable range of X_{rec} when applying control of D_2, namely a wider range of dc output voltage regulation [refer to the following section]. Note that $Z_{norm}(C_r)$ influences X_{rec} more obviously.

In practice, the final dc load R_L may change over a wide range. As shown in Fig. 6(e)(f), a small R_L, i.e., large $Z_{norm}(C_{Q_r})$ and $Z_{norm}(C_{D_r})$, leads to high voltage stress on Q_r and D_r. Thus, under specific voltage rating of Q_r and D_r, a starting point for designing C_{Q_r} and C_{D_r} is to be based on the smallest target R_L [refer to (23) and (24)]. Again, the value of C_r significantly impacts the rectifier input impedance. It can be determined based on the target rectifier input resistance, R^*_{rec}, under rated dc load and rated output power [refer to Fig. 6(g), (7), (11), (15), and (20)].

$$v_{Dr,peak} = \frac{1}{\omega(C_r + C_{Dr})} [I_m \cos(2\pi D_1 + \phi_{rec}) \\ -I_m \cos(2\pi D_2 + \phi_{rec}) + 2\pi I_o(D_1 - D_2)], \tag{23}$$

$$v_{Qr,peak} = \frac{1}{1 + \frac{C_{Qr}}{C_r} + \frac{C_{Qr}}{C_{Dr}}} \left\{ \frac{I_m}{\omega C_r} [\cos(2\pi D_2 + \phi_{rec}) \\ - \cos(2\pi D_3 + \phi_{rec})] + \frac{1}{\omega C_{Dr}} (2\pi I_o(D_3 - D_2)) \right\}. \tag{24}$$

In addition, to further investigate the soft-switching operation and parameter design of the active rectifier, the drain-source voltages of Q_r and D_r are shown in Fig. 7 under largely varying rectifier parameters C_{Qr} and C_{Dr}, dc load R_L, and amplitude of rectifier input current I_m. Note that in Fig. 7(a)-(d) V_o's are all 10 V. The figure shows that the active rectifier can maintain the soft-switching operation (zero-voltage-switching here) of Q_r and D_r under a wide range of R_L and I_m. It also can be seen that lower C_{Qr} and C_{Dr} help better achieve the soft-switching operation of the active rectifier, but also lead to higher voltage stress on Q_r and D_r. This observation is consistent with the results in Fig. 6(e) and (f).

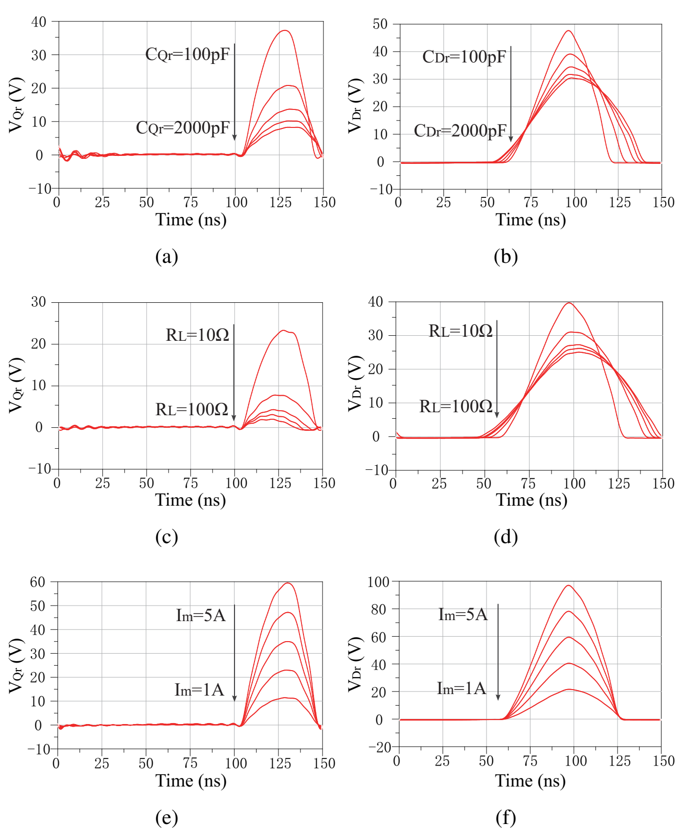

Fig. 7. Investigation of soft-switching operation of the active rectifier. (a) V_{Q_r} vs. C_{Qr}. (b) V_{D_r} vs. C_{Dr}, (c) V_{Q_r} vs. R_L. (d) V_{D_r} vs. R_L. (e) V_{Q_r} vs. I_m. (f) V_{D_r} vs. I_m.

Based on the above analysis and discussion, the below guidelines are summarized to select C_r, C_{Q_r}, and C_{D_r} in the active Class E rectifier:

1) The small C_{D_r} and C_{Q_r} could be used to avoid the short duration of mode 4, and thus guarantee the soft-switching operation. However, it will lead to higher voltage stress on switch Q_r and diode D_r. As discussed above, C_{D_r} and C_{Q_r} should be determined based on the voltage rating of the diode D_r and the MOSFET Q_r and the smallest target R_L.
2) The value of C_r should be chosen based on the target nominal rectifier input resistance. It influences the reflected impedance on the transmitting side and thus power transfer capability of the MHz WPT system.
3) The values of C_{Q_r}, C_{D_r}, and C_r should be finalized to achieve a balanced design taking into account the different criteria, such as soft-switching operation, switch voltage stress, power transfer capability, and also available products on market.

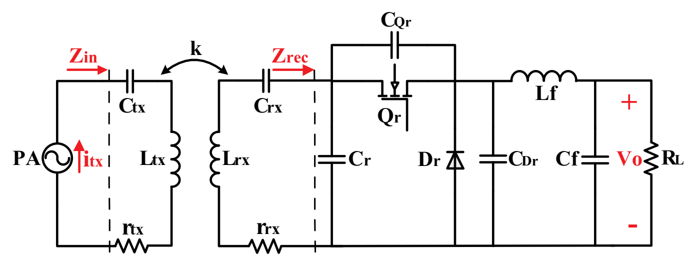

Fig. 8. An example MHz WPT system using active Class E rectifier.

III. Output Voltage Regulation

The above 6.78-MHz WPT system in Fig. 8 serves as a general example to analyze and explain the dc output voltage (i.e., V_o) regulation through the active Class E rectifier. This example system consists of a power amplifier (PA), a pair of coupling coils, the active Class E rectifier, and a final dc load. In Fig. 8, L_{tx} and r_{tx}, L_{rx} and r_{rx}, are self-inductances and self-resistances of the transmitting and receiving coils, respectively; i_{tx} is the input current of the transmitting coil; Z_{in} and Z_{rec} are the input impedances of the coupling coils and rectifier; L_m is mutual inductance,

$$L_m = k\sqrt{L_{tx}L_{rx}}, \tag{25}$$

where k is the mutual inductance coefficient. To improve efficiency and power transfer capability, C_{tx} and C_{rx} are usually designed as follows,

$$j\omega L_{rx} + \frac{1}{j\omega C_{rx}} = 0, \tag{26}$$

$$j\omega L_{tx} + \frac{1}{j\omega C_{tx}} = 0, \tag{27}$$

where ω is the operating frequency of the WPT system, 6.78 MHz here. The input impedance of the coupling coils, $Z_{in}(= R_{in} + jX_{in})$, can then be derived as

$$R_{in} = \frac{\omega^2 {L_m}^2 (R_{rec}+r_{rx})}{(R_{rec}+r_{rx})^2 + {X_{rec}}^2} + r_{tx}, \tag{28}$$

$$X_{in} = -\frac{\omega^2 {L_m}^2 X_{rec}}{(R_{rec}+r_{rx})^2 + (X_{rec})^2}. \tag{29}$$

Thus the output power of the rectifier is

$$P_o = \frac{I_{tx}^2}{2} \cdot \frac{\omega^2 k^2 L_{tx} L_{rx} R_{rec}}{(R_{rec}+r_{rx})^2 + {X_{rec}}^2} \cdot \eta_{rec}, \tag{30}$$

where I_{tx} is the magnitude of i_{tx}, and the rectifier efficiency η_{rec} can be calculated as

$$\eta_{rec} = \frac{I_o^2 R_L}{I_o^2 R_L + I_o^2 r_{L_f} + P_{Loss,Q_r} + P_{Loss,D_r}}, \tag{31}$$

where

$$P_{Loss,Q_r} = \frac{1}{2\pi} \int_0^{2\pi} i_{Q_r}^2 r_{DS} d\omega t, \tag{32}$$

$$P_{Loss,D_r} = \frac{1}{2\pi} \int_0^{2\pi} i_{D_r} V_F d\omega t. \tag{33}$$

Here r_{Lf}, r_{DS}, and V_F are the ESR of inductor L_f, on-resistance of MOSFET Q_r, and forward voltage drop of diode D_r, respectively.

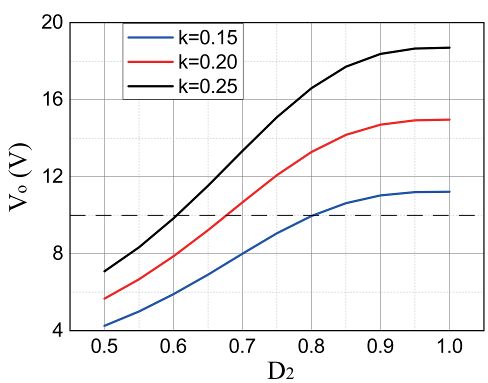

Fig. 9. Output voltage V_o versus D_2 and k.

Finally, the dc output voltage of the WPT system is

$$V_o = \sqrt{R_L P_o} = \omega k I_{tx} \sqrt{\frac{R_L L_{tx} L_{rx} R_{rec}}{2[(R_{rec}+r_{rx})^2 + {X_{rec}}^2]}} \eta_{rec}. \tag{34}$$

As shown in the above equation, V_o is determined by the mutual inductance k, dc load R_L, and rectifier input impedance $Z_{rec}(= R_{rec} + jX_{rec})$. Note that R_{rec} and X_{rec} relate to D_1, D_2, and D_3 [refer to (20)(21) and Fig. 5]. Again, D_1 and D_3, the two equivalent duty cycles, are determined by the actual duty cycle D_2. Fig. 5 illustrates that Z_{rec} can be tuned through the duty cycle control (i.e., D_2) of the switch Q_r. Through this approach, the output voltage of the overall WPT system can be regulated eliminating the need of an additional regulating circuit. Fig. 9 shows V_o under different k and D_2, which is calculated using the parameters in Table IV. These parameters are from the final experimental system discussed in next section. Under a changing k, i.e., variation in coil relative position, a stable V_o can be achieved by having a proper D_2. For instance, with D_2=0.80, 0.68, 0.61, a fixed output voltage (10 V) is maintained under different k=0.15, 0.2, and 0.25, respectively [see the dashed line in Fig. 9].

TABLE IV
PARAMETERS OF EXPERIMENTAL WPT SYSTEM.

L_{tx} (μH)	L_{rx} (μH)	r_{tx} (Ω)	r_{rx} (Ω)
1.47	1.47	0.3	0.3
I_{tx} (A)	C_r (pF)	C_{Q_r} (pF)	C_{D_r} (pF)
2	400	400	400

Note (34) can be rewritten as

$$k = \frac{V_o}{\omega I_{tx}} \sqrt{\frac{2}{R_L L_{tx} L_{rx}}} Z_x, \tag{35}$$

where

$$Z_x \doteq \sqrt{\frac{(R_{rec} + r_{rx})^2 + X_{rec}^2}{R_{rec}\eta_{rec}}}. \tag{36}$$

The range of the mutual inductance coefficient, k, in which a target output voltage can be maintained, is then derived as

$$\frac{V_o}{\omega I_{tx}} \sqrt{\frac{2}{R_L L_{tx} L_{rx}}} Z_x^{min} \le k \le \frac{V_o}{\omega I_{tx}} \sqrt{\frac{2}{R_L L_{tx} L_{rx}}} Z_x^{max}. \tag{37}$$

Again, Z_x is tuned by D_2. The range of the output voltage under a specific k can be similarly derived, which is reversely proportional to the range of Z_x. For instance, with the parameters in Tables II and IV, the regulated maximum V_o's under small k's are listed in Table V, which are all lower than 10 V.

TABLE V
REGULATED MAXIMUM V_o VERSUS k.

k	0.13	0.11	0.09	0.07	0.05
V_o^{max} (V)	9.72	8.23	6.73	5.23	3.74

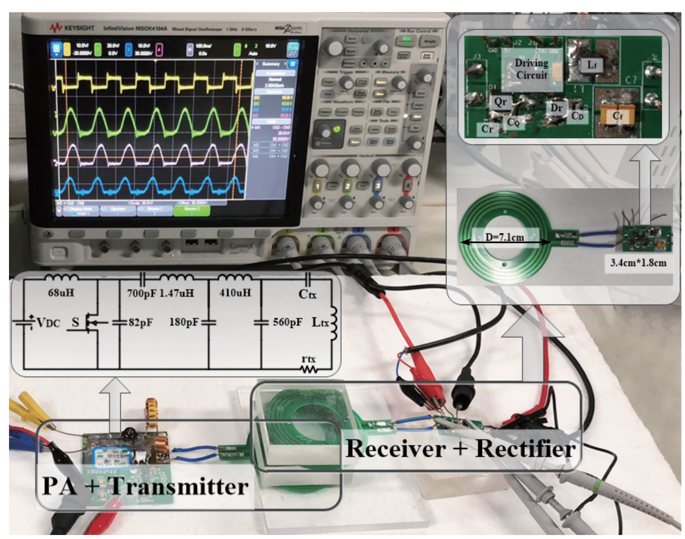

Fig. 10. An experimental 6.78-MHz WPT system employing active Class E rectifier.

IV. EXPERIMENTAL VERIFICATION

An experimental 6.78-MHz WPT system is built up employing the proposed active Class E rectifier. As shown in Fig. 10, this experimental WPT system includes a current model (CM)

Class E PA, transmitting and receiving coils, and active Class E rectifier. A 10 Ω dc load is emulated using an electronic load. The CM Class E PA uses a π matching network to achieve a constant PA output current against varying load impedance such as due to variation in coil relative position [see the circuit model in Fig. 10] [15]. In the active rectifier, a Schottky silicon carbide diode (DFLS240) works as the rectifying diode D_r, and the switch Q_r is implemented using a MOSFET (FDMC8884). Major parameters of the experimental system are listed in Table IV. Design parameters of the rectifier, C_r, C_{Q_r}, and C_{D_r}, are chosen based on specifications of the switching devices and design guidance in Section II-C.

Fig. 11 shows experimental waveforms of the MOSFET gate driving voltage V_{gs}, rectifier input voltage v_{rec}, MOSFET drain-source voltage v_{Q_r}, and voltage across diode v_{D_r} under different duty cycle of the switch Q_r (i.e., different D_2). Here dc input voltage of the Class E PA V_{dc} is 40 V and the mutual inductance coefficient k=0.146. It shows that v_{Qr} and v_{Dr} decrease and increase, respectively, when the duty cycle D_2 increases from 0.5 to 1, and the dc output voltage of the active rectifier is regulated from 4.5 V to 13.1 V [refer to Fig. 16]. Both the MOSFET and diode operate with soft switching.

Fig. 12 shows the experimental duty cycle D_2 during the output voltage regulation. The target constant output voltage V_o is 10 V and k varies from 0.146 to 0.245. The variation in k can be implemented by adjusting misalignment and/or distance between the coupling coils. The parameter k is measured by the vector network analyzer. When k changes, the duty cycle D_2 is tuned accordingly based on the detection of the output voltage, and thus this voltage can be regulated. In the figure, a higher k requires a smaller duty cycle D_2 in order to maintain the 10 V constant output voltage V_o. It is because that a higher k leads to a higher reflected resistance R_{in} on the transmitting side, and thus higher power delivered to the receiving side thanks to the CM Class E PA. Thus a lower D_2 is required to reduce R_{in} and transferred power through the coupling coils. Calculation results are also given in Fig. 12 to validate the above analytical analysis and derivations. Fig. 13 demonstrates that the CM Class E PA works as a current source to provide a relatively constant current, I_{tx}, with the varying k. I_{rec} decreases (i.e., a smaller D_2) with a higher k in order to maintain the constant 10 V output voltage V_o.

Fig. 14 gives the experimental results of the rectifier efficiency and system efficiency under the output voltage regulation. The ac input power of the rectifier is measured by using voltage and current probes of the oscilloscope. In order to achieve a high-accuracy measurement, the voltage and current probes are calibrated for the same phase at 6.78 MHz. The active rectifier can achieve up to 94% efficiency when the output voltage is regulated to be 10 V with the varying k. The decreased system efficiency with an increasing k is mainly caused by the lower PA efficiency because of the increased reflected reactance X_{in}. Fig. 15 shows the output voltage with/without voltage regulation versus k. The experiment without voltage regulation is implemented by fixing $D_2 = 1$.

Fig. 16 provides both experimental and calculation results of the output voltage V_o when sweeping D_2 and with a constant $k = 0.2$. V_o varies from 4.5 V to 13.1 V when D_2 is controlled to change from 0.5 to 1. Good match between the two results validates the correctness of (34) derived in section III. This equation is important to predict and guide the design of output voltage tunable range of the active Class E rectifier in future MHz WPT applications.

Fig. 17 shows the experimental results of the rectifier efficiency and system efficiency when sweeping D_2 and under a constant $k = 0.2$. The rectifier efficiency improves with a higher D_2 and thus larger output power P_o (2–17 W here). From Fig. 5 and (28), it can be seen that a lower D_2 leads to a smaller reflected resistance R_{in}, namely higher power loss in the transmitting coil. This explains the low system efficiency when the duty cycle D_2 is small.

TABLE VI
LOSS BREAKDOWN OF ACTIVE RECTIFIER (%).

D_2	$P_{Q_r(sw)}$	$P_{Q_r(cd)}$	$P_{Q_r(gate)}$	P_{D_r}	P_{L_f}
0.70	7.4%	9.4%	19.0%	52.4%	11.8%
0.75	7.5%	9.9%	16.1%	53.3%	13.2%
0.80	9.2%	9.7%	13.9%	53.1%	14.1%
0.85	10.8%	9.3%	12.9%	52.6%	14.4%

For reference purposes, Table. VI lists the loss breakdown of the active rectifier when the voltage is regulated at 10 V by tuning D_2 from 0.70 to 0.85 [refer to Fig.12]. $P_{Q_r(sw)}$, $P_{Q_r(cd)}$, and $P_{Q_r(gate)}$ are the switching loss, conduction loss, and gate drive loss of the MOSFET Q_r, respectively. P_{D_r} and P_{L_f} are the power loss on the diode D_r and the inductor L_f. The power losses are calculated based on the measured currents and components parasitics. The results show that the switching loss of Q_r is not significant thanks to the soft-switching operation, and the diode power loss is dominant due to its high forward voltage drop (about 0.45 V). The percentage of the gate driving loss decreases under the increasing duty cycle D_2 due to the increasing output power.

V. CONCLUSIONS

This paper proposes a Class E-based active rectifier for high-frequency rectification and dc output voltage regulation in MHz WPT systems. Its behavior is analytically explained under different combination of on/off states of the switch and diode, namely the four operation modes. Guidance on selecting rectifier design parameters is also developed to compromise among efficiency (i.e., soft-switching operation), switch voltage stress, and tunable range of impedance. The dc output voltage is further derived analytically to establish its relationship with the duty cycle control of the active rectifier. Both calculation and experimental results well validate the analytical analysis, high-efficiency and output voltage regulation capability of the proposed active Class E rectifier.

REFERENCES

[1] J. Shin, S. Shin, Y. Kim, S. Ahn, S. Lee, G. Jung, S. Jeon, and D. Cho, "Design and implementation of shaped magnetic-resonance-based wireless power transfer system for roadway-powered moving electric vehicles," *IEEE Trans. Ind. Electron.*, vol. 61, no. 3, pp. 1179–1192, Mar. 2014.

[2] R. Hua and P. A. Hu, "Modelling and analysis of inductive power transfer system with passive matrix power repeater," *IEEE Trans. Ind. Electron.*, DOI 10.1109/TIE.2018.2860560, to be published.

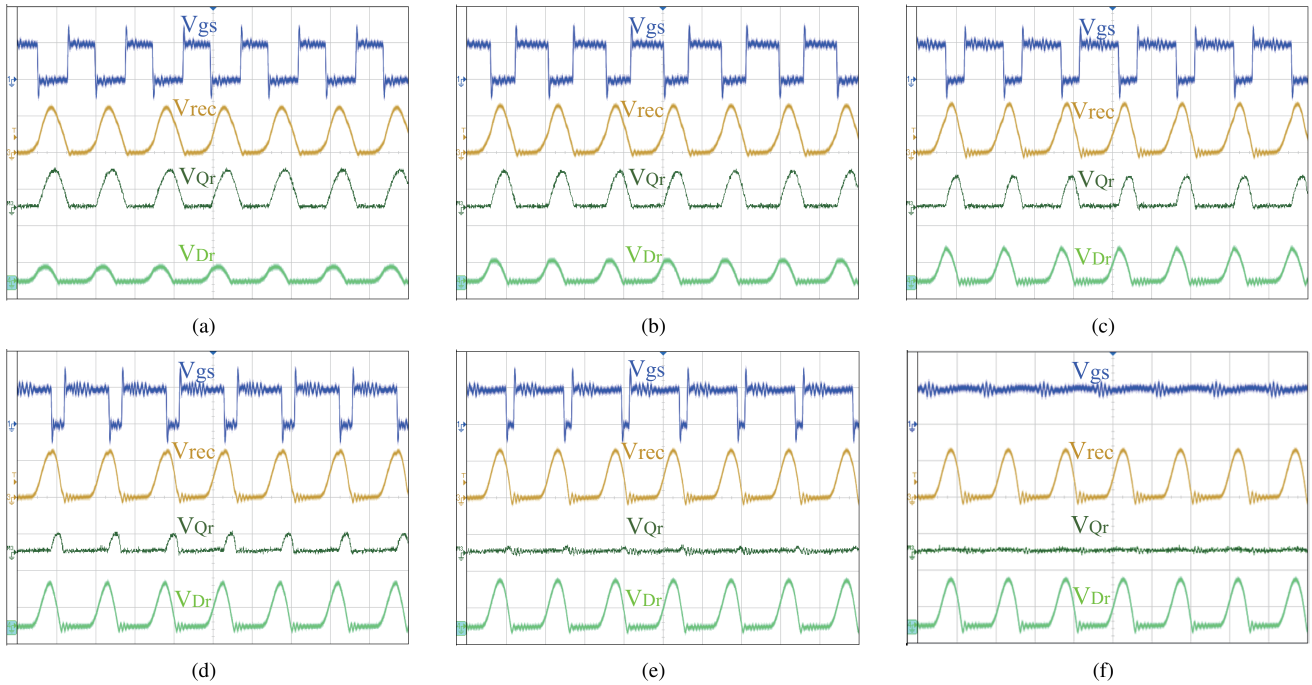

Fig. 11. Experimental waveforms of V_{gs} (5 V/div.), V_{rec} (30 V/div.), V_{Q_r} (30 V/div.), V_{D_r} (30 V/div.) under different duty cycle D_2. (a) $D_2 = 0.5$. (b) $D_2 = 0.6$. (c) $D_2 = 0.7$. (d) $D_2 = 0.8$. (e) $D_2 = 0.9$. (f) $D_2 = 1$.

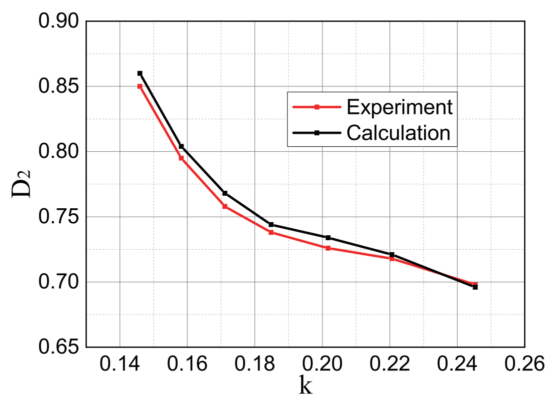

Fig. 12. Duty cycle D_2 versus k for 10 V output voltage regulation.

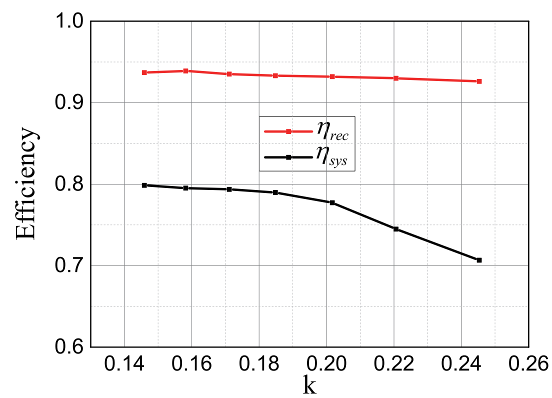

Fig. 14. Rectifier and system efficiencies, η_{rec} and η_{sys}, versus k during 10 V output voltage regulation.

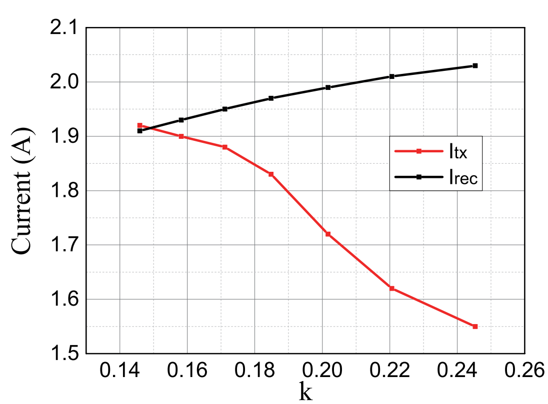

Fig. 13. Current magnitudes I_{tx} and I_{rec} for 10 V output voltage regulation.

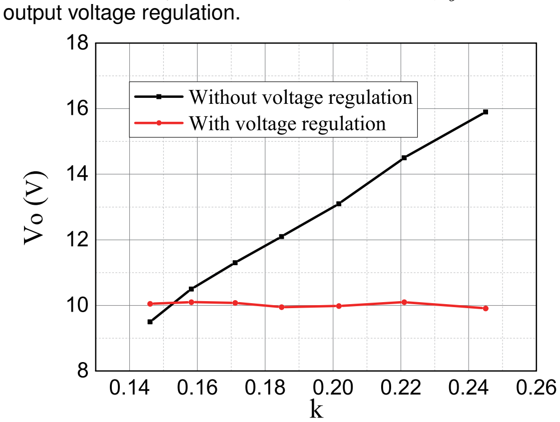

Fig. 15. Output voltage with/without voltage regulation versus k.

[3] T. Kan, T. Nguyen, J. C. White, R. K. Malhan, and C. C. Mi, "A new integration method for an electric vehicle wireless charging system using

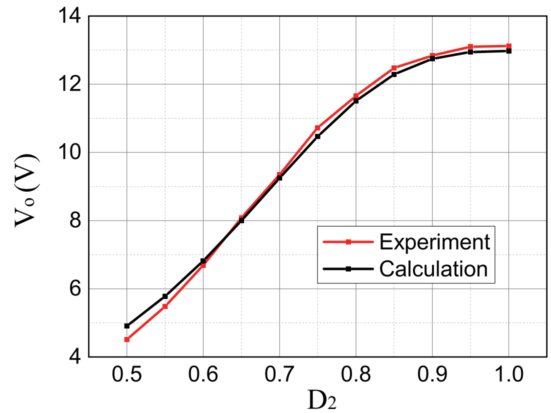

Fig. 16. Rectifier output voltage V_o versus D_2.

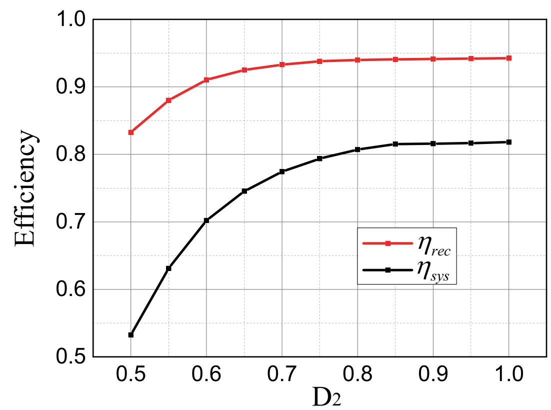

Fig. 17. Rectifier and system efficiencies, η_{rec} and η_{sys}, versus D_2.

LCC compensation topology: Analysis and design," *IEEE Trans. Power Electron.*, vol. 32, no. 2, pp. 1638–1650, Feb. 2017.

[4] C. C. Mi, G. Buja, S. Y. Choi, and C. T. Rim, "Modern advances in wireless power transfer systems for roadway powered electric vehicles," *IEEE Trans. Ind. Electron.*, vol. 63, no. 10, pp. 6533–6545, Oct. 2016.

[5] A. Kurs, A. Karalis, R. Moffatt, J. D. Joannopoulos, P. Fisher, and M. Soljačić, "Wireless power transfer via strongly coupled magnetic resonances," *science*, vol. 317, no. 5834, pp. 83–86, 2007.

[6] S. Hui, W. Zhong, and C. Lee, "A critical review of recent progress in mid-range wireless power transfer," *IEEE Trans. Power Electron.*, vol. 29, no. 9, pp. 4500–4511, Sep. 2014.

[7] J. Choi, D. Tsukiyama, Y. Tsuruda, and J. M. Rivas, "High-frequency, high-power resonant inverter with eGaN FET for wireless power transfer," *IEEE Trans. Power Electron.*, vol. 33, no. 3, pp. 1890–1896, Aug. 2017.

[8] M. Liu, M. Fu, and C. Ma, "Parameter design for a 6.78-MHz wireless power transfer system based on analytical derivation of Class E current-driven rectifier," *IEEE Trans. Power Electron.*, vol. 31, no. 6, pp. 4280–4291, Jun. 2016.

[9] C. Zhao and D. Costinett, "GaN-based dual-mode wireless power transfer using multifrequency programmed pulse width modulation," *IEEE Trans. Ind. Electron.*, vol. 64, no. 11, pp. 9165–9176, Nov. 2017.

[10] T. C. Beh, M. Kato, T. Imura, S. Oh, and Y. Hori, "Automated impedance matching system for robust wireless power transfer via magnetic resonance coupling," *IEEE Trans. Ind. Electron.*, vol. 60, no. 9, pp. 3689–3698, Sep. 2013.

[11] S. Aldhaher, D. C. Yates, and P. D. Mitcheson, "Design and development of a Class EF_2 inverter and rectifier for multimegahertz wireless power transfer systems," *IEEE Trans. Power Electron.*, vol. 31, no. 12, pp. 8138–8150, Dec. 2016.

[12] J. M. Arteaga, S. Aldhaher, G. Kkelis, D. C. Yates, and P. D. Mitcheson, "Multi-MHz IPT systems for variable coupling," *IEEE Trans. Power Electron.*, vol. 33, no. 9, pp. 7744–7758, Sep. 2018.

[13] M. Fujii, T. Suetsugu, K. Shinoda, and S. Mori, "Class-E rectifier using thinned-out method," *IEEE Trans. Power Electron.*, vol. 12, no. 5, pp. 832–836, Sep. 1997.

[14] S. Aldhaher, P.-K. Luk, K. El Khamlichi Drissi, and J. Whidborne, "High-input-voltage high-frequency Class E rectifiers for resonant inductive links," *IEEE Trans. Power Electron.*, vol. 30, no. 3, pp. 1328–1335, Mar. 2015.

[15] S. Liu, M. Liu, S. Yang, C. Ma, and X. Zhu, "A novel design methodology for high-efficiency current-mode and voltage-mode Class-E power amplifiers in wireless power transfer systems," *IEEE Trans. Power Electron.*, vol. 32, no. 6, pp. 4514–4523, Jun. 2017.

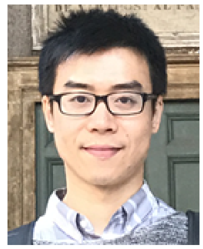

Ming Liu (S'15-M'17) received the B.S. degree in mechatronic engineering from Sichuan University, Sichuan, China, in 2007, and the Ph.D. degree in electrical and computer engineering from the University of Michigan-Shanghai Jiao Tong University Joint Institute, Shanghai Jiao Tong University, Shanghai, China, in 2017. He is currently a postdoctoral research fellow at Department of Electrical Engineering, Princeton University, Princeton, NJ, USA. His research interests include circuit topologies and architectures, control strategies, parameters design and optimization of megahertz wireless power transfer systems as well as high frequency power electronics.

Dr. Liu serves as Guest Editor of IEEE Transactions on Industrial Informatics and Chair of the Wireless Charging Subcommittee of Energy Storage Technical Committee, IEEE Industrial Electronics Society. He received Top Ten Academic Star Award and Excellent PhD Thesis Award Nomination at Shanghai Jiao Tong University in 2016 and 2018, and Research Excellence Award from AirFuel Alliance, USA, in 2019.

Jibin Song (S'16) received the B.S. degree in measurement & control technology and instrumentation from Jilin University, Jilin, China, in 2016. He is currently working toward the Ph.D. degree in electrical and computer engineering, University of Michigan-Shanghai Jiao Tong University Joint Institute, Shanghai Jiao Tong University, Shanghai, China. His research interests include general power electronics, design and optimization of megahertz wireless power transfer systems such as multiple-receiver systems and high efficiency rectification.

Chengbin Ma (M'05-SM'18) received the B.S. degree in industrial automation from East China University of Science and Technology, Shanghai, China, in 1997, and the M.S. and Ph.D. degrees in electrical engineering from The University of Tokyo, Tokyo, Japan, in 2001 and 2004, respectively. From 2004 to 2006, he was an R&D Researcher with the Servo Motor Laboratory, FANUC Limited, Japan. Between 2006 and 2008, he was a Postdoctoral Researcher with the Department of Mechanical and Aeronautical Engineering, University of California, Davis, USA. He joined the University of Michigan-Shanghai Jiao Tong University Joint Institute (UM-SJTU Joint Institute), Shanghai Jiao Tong University, Shanghai, China, in 2008, and currently an Associate Professor of electrical and computer engineering. His research interests include energy management, megahertz wireless power transfer, dynamics and motion control, and wide applications in electronic devices, electric vehicles, microgrids, smart grids, etc.

Dr. Ma is an IEEE senior member. He serves as Delegate of Energy Cluster, Chair of Energy Storage Technical Committee and Chair of Shanghai Chapter, IEEE Industrial Electronics Society. He is an Associated Editor for the IEEE Transactions on Industrial Informatics. He and his supervised students won many teaching and research awards at Shanghai Jiao Tong University, such as Koguan Top Ten Best Teacher Award in 2017 and Koguan Top Ten Research Group Award in 2014. He also received Research Excellence Award from AirFuel Alliance, USA, in 2019.